Improved algorithm for determining the Visible Infrared Imaging Radiometer Suite Day/Night Band high-gain stage dark offset free from light contamination

Yalong Gu,[1,*] Sirish Uprety,[2] Slawomir Blonski,[1] Bin Zhang,[2] and Changyong Cao[3]

[1]Global Science & Technology, Inc., Greenbelt, Maryland 20770, USA
[2]Cooperative Institute for Climate and Satellites, Earth System Science Interdisciplinary Center, University of Maryland, College Park, Maryland 20740, USA
[3]Center for Satellite Applications and Research, NOAA/NESDIS, College Park, Maryland 20740, USA
*Corresponding author: yalong.gu@noaa.gov

Dark offset is one of the key parameters for Visible Infrared Imaging Radiometer Suite (VIIRS) Day/Night Band (DNB) high-gain stage (HGS) radiometric calibration, whose accuracy strongly impacts applications of DNB low-light detection for Earth observation at nighttime. Currently, DNB observation of the VIIRS onboard calibrator blackbody (OBCBB) view, together with its observation of deep space during the spacecraft pitch maneuver performed early in the mission, has been used to compute the HGS dark offset continuously. However, the relationship between the DNB OBCBB data and the Earth view (EV) data is unclear due to electronic timing differences between these two views. It is questionable whether the DNB OBCBB data can monitor the EV HGS dark offset change. Through comprehensive analysis of the DNB OBCBB data and EV data acquired from the monthly special acquisitions known as the VIIRS recommended operating procedures (VROPs), we have shown that the OBCBB data can only track the dark current component of the DNB HGS EV dark offset, instead of the total dark offset. The DNB observation of deep space during the spacecraft pitch maneuver was also contaminated by starlight. With such background, in this paper we propose an improved algorithm for determining the DNB HGS dark offset. By combined use of the DNB OBCBB data and the DNB VROP data, the generated DNB HGS dark offset is both free from light contamination and capable of tracking continuous drift. The improved algorithm could potentially improve the DNB radiometric performance at low radiance level. Our results provide a solid theoretical basis for dark offset calibration of the VIIRS DNB onboard Suomi National Polar-Orbiting Partnership satellite and the following Joint Polar Satellite System satellites.

1. INTRODUCTION

The Day/Night Band (DNB) is a panchromatic visible and near-infrared band of theVisible Infrared Imaging Radiometer Suite (VIIRS) on board the Suomi National Polar-Orbiting Partnership (S-NPP) satellite. Benefiting from its three gain stage design, i.e., the low-gain stage (LGS) for daytime scenes, the mid-gain stage (MGS) for twilight scenes, and the high-gain stage (HGS) for nighttime low-light scenes, the DNB is capable of quantitative measurement of light radiances from 3×10^{-9} W · cm^{-2} · sr^{-1} to 2×10^{-2} W · cm^{-2} · sr^{-1}, a range sufficiently wide for both day and night Earth observations [1]. Evaluation of its on-orbit performance showed that the DNB's minimum detectable radiance is around 2×10^{-10} W · cm^{-2} · sr^{-1} [2]. Such extreme sensitivity to low lights enables new capabilities of environmental remote sensing [3,4]. The global low-light imaging data collected by the DNB has also been successfully used to generate science-grade global nighttime light maps [5,6], a product for broad applications such as monitoring of anthropogenic activities [7] and automatic fishing boat detection [8].

Quality of the DNB low-light detection for Earth observation in nighttime relies on the calibration accuracy. The DNB is calibrated via a linear calibration equation where dark offset and gain are two key parameters. Determination of dark offset is

critical, since any bias in dark offset will propagate to the calibrated radiance through the calibration equation. In addition, dark offset is a prerequisite for gain determination. Currently, DNB observations collected over the Pacific Ocean during nighttime of the new moon through the Earth view (EV) are selected for dark offset evaluation. These data are acquired once every lunar month through a special process known as the VIIRS recommended operating procedure (VROP) [9].

The DNB is effectively an integration of three separate imagers, namely, its LGS, MGS, and HGS, which have the same spectral range but observe the Earth independently. Although the LGS and MGS dark offset determined from the data acquired during VROPs are satisfactory for radiometric calibration of these two stages, the HGS dark offset determined from the corresponding HGS VROP data is overestimated due to contributions from airglow in the Earth middle atmosphere [10]. Recently, an alternative method has been developed to correct such airglow-induced bias. The method first determines the baseline HGS dark offset by the DNB observation of deep space collected during the spacecraft pitch maneuver early in the mission and then tracks its on-orbit drift due to radiation damage from energetic particles in the space environment by the onboard calibrator blackbody (OBCBB) data collected when the spacecraft is in Earth eclipse and the Moon is less than quarter phase [11,12,13,14]. Since there is no atmosphere in deep space view, the derived HGS dark offset is free from airglow.

Compared to the original method of the DNB HGS dark offset determination by the monthly VROPs, a significant change of the alternative method is the involvement of the OBCBB. Unlike the VROP data, the DNB OBCBB data are collected in real time without special VROP protocols. The alternative method can be run automatically, and the DNB HGS dark offset can be updated much more frequently than the monthly update through the VROPs. However, this *algorithm* relies on an assumption that the DNB OBCBB data can monitor the EV HGS dark offset change. To the best of our knowledge, this precondition has not been validated. In particular, the relationship between the DNB EV and OBCBB data is unclear due to electronic timing differences between two views [15]. Characterization of this relationship is necessary for any DNB dark offset calibration algorithms that use the OBCBB data.

This paper is devoted to answering the fundamental question. Through a comprehensive analysis, we show that the DNB OBCBB data can only track the *dark current* component of the DNB HGS EV dark offset, instead of the *total dark offset*. In this paper, we propose a new and improved algorithm for determining the DNB HGS dark offset that is both free from light contamination and capable of tracking continuous drift. Comparison with the DNB HGS dark offset computed by the aforementioned algorithm using the DNB pitch maneuver data also shows that the DNB observation of deep space during the spacecraft pitch maneuver was contaminated by starlight. The improved algorithm could potentially improve the DNB radiometric performance at low radiance level. Our results provide a solid theoretical basis for dark offset calibration of the VIIRS DNB onboard S-NPP satellite and the following Joint Polar Satellite System satellites.

The paper is organized as follows. The VIIRS DNB and its dark offset calibration are described in Section 2. The DNB OBCBB data is comprehensively analyzed in Section 3 to reveal its role in tracking the DNB HGS dark offset drift. Our improved algorithm that can generate the DNB HGS dark offset free from light contamination is proposed in Section 4. Discussions and conclusions are given in Section 5.

2. OVERVIEW OF VIIRS DNB AND ITS DARK OFFSET CALIBRATION

The VIIRS DNB sensor is a temperature controlled charge-coupled device (CCD) composed of four detector arrays named high-gain stage A (HGA), high-gain stage B (HGB), MGS, and LGS, according to their ranges of detectable radiance. Their sizes (track × scan) are 672 × 250, 672 × 250, 672 × 3, and 672 × 1, respectively. The redundant detectors along the scan direction of HGA and HGB allow repeated measurement of the same target. This is the so-called time delay integration (TDI) [15], which effectively extends the integration time and thereby enhances sensitivity to low-light signals. In practice, the HGA and HGB are combined to form a single output known as HGS for Earth observations.

On orbit, the DNB, as well as other VIIRS bands, collects data via a rotating telescope assembly and a two-side half-angle mirror (HAM) that scans four windows of view—EV, OBCBB, solar diffuser (SD), and space view (SV)—successively (Ref. [15], Fig. 7). The latter three are known as the onboard calibrators designed for the VIIRS on-orbit calibration [16]. The EV window of the DNB is divided into 32 aggregation zones on each side of nadir. The aggregation zones are a function of scan position at which a different number of detectors is grouped according to the specific aggregation mode (Ref. [17], Table 3.3-6) to provide nearly constant ground resolution over the entire DNB swath, which is approximately 742 m pixel size. After aggregation, the size of a single-scan DNB EV data is 16 × 4064 (track × scan). The 16 along-track pixels are created by onboard aggregation of 672 along-track detectors. Unless otherwise specified, the actual detectors are named as "subpixels," while the term "detector" used in the rest of the paper is referred to as such 16 virtual along-track detectors, both following the VIIRS nomenclature [15]. Unlike the DNB EV data whose 4064 pixels of a scan include all 32 aggregation modes, the DNB OBC data (BB, SD, and SV) are only recorded in an aggregation mode per scan, while the aggregation scheme that controls subpixel grouping is the same for both the EV and the OBC views.

The original algorithm for the DNB dark offset calibration is straightforward. The Pacific Ocean in nighttime of a new moon is selected as a dark target for the DNB. Its dark scenes are collected by the DNB's three gain stages separately during monthly VROPs. After processing the recorded data with a proper filtering scheme to remove bright lights, dark offsets are generated. The size of these dark offsets is 16 detectors ×4064 samples ×2 HAM sides [9]. These dark offsets can be used for DNB EV calibration directly, thereafter referred to as EV dark offsets.

It was soon discovered that the dark Earth scenes collected during VROPs include airglow that can be detected by the DNB HGS [3], resulting in overestimated HGS dark offset

for its EV calibration. Since there is no atmosphere in deep space view, a baseline HGS dark offset, free from airglow, was determined by the DNB EV scenes of deep space collected during the spacecraft pitch maneuver early in the mission. Upon tracking on-orbit change through the DNB OBCBB data, the HGS dark offset at a given time is obtained, expressed by the following equation [18] as

$$\begin{aligned} &\text{HGS\_dark\_offset\_EV}(\text{det}, \text{sample}, \text{ham}, t) \\ &= \text{HGS\_dark\_offset\_EV}_0(\text{det}, \text{sample}, \text{ham}) \\ &\quad + [\text{HGS\_dark\_offset\_trend\_BB}(\text{det}, \text{agg}, \text{ham}, t) \\ &\quad - \text{HGS\_dark\_offset\_trend\_BB}(\text{det}, \text{agg}, \text{ham}, t_0)], \end{aligned} \quad (1)$$

where det, ham, and agg denote the detector, HAM side, and aggregation mode. $\text{HGS\_dark\_offset\_EV}_0$ is the baseline EV HGS dark offset using the PM data collected on 20 February 2012. HGS_offset_trend_BB tracks the on-orbit change of the HGS dark offset using the OBCBB data. The OBCBB operates with nominal temperature of 292.5 K. According to Planck's law, its emitted radiance in the DNB spectral range is undetectable even by the HGS. Therefore it is a suitable dark target for the DNB.

Analysis of the DNB OBCBB data shows that both of its HGS and MGS measurements are elevated during daytime, probably due to light that enters through the EV window and then reaches the OBCBB. The BB dark offset of the DNB is obtained by processing the DNB OBCBB data collected when the spacecraft is in Earth eclipse. In principle, the BB dark offset can be determined for every orbit. A one-day window including 14 orbits is usually used to obtain smoothed BB dark offset [11]. Because the HGS OBCBB data is contaminated by the moonlight that reaches the BB through the EV window, the time series of the daily BB HGS dark offset shows periodic peaks that correlate with the cycle of lunar phases [12,14]. In order to eliminate moonlight contamination, only the BB HGS dark offsets determined around a new moon are used to generate continuous trend HGS_offset_trend_BB through a linear fit [12,18]. The on-orbit change of EV HGS dark offset at given time t with respect to the time of pitch maneuver t_0 is computed by the change of HGS_offset_trend_BB during this time period.

It should be noted that the DNB BB dark offset for each gain stage is determined per aggregation mode. All samples of the EV HGS dark offset that belong to the same aggregation mode experience the same change, as illustrated by Eq. (1). The relationship between 4064 along-scan EV samples and 32 aggregation modes can be derived from the DNB aggregation scheme (Ref. [17], Table 3.3-6). The algorithm outlined by Eq. (1) is referred to as the pitch maneuver (PM) based algorithm in this paper.

3. RELATIONSHIP BETWEEN DNB EV AND BB HGS DARK OFFSET

Although the PM based algorithm can be run automatically and update the DNB EV HGS dark offset frequently by using the BB HGS dark offset, it is unclear whether the BB HGS dark offset can monitor the EV HGS dark offset drift over time considering the electronic timing difference when the DNB electronics reads data from the OBCBB and the EV. This is a key question that must be answered before using the DNB OBCBB data for any EV dark offset calibration algorithms. In this section, we investigate the relationship between the DNB EV and BB dark offset through in-depth analysis of the DNB VROP and OBCBB data.

To begin with, we introduce the definition of CCD dark offset. It is evaluated through measurement of dark targets, namely dark images. A CCD dark image usually contains three main components: thermal dark charge, offset level, and fixed pattern noise [19]. Thermal dark charge, also known as dark current, is referred to as free electrons generated in a CCD sensor by thermal energy. Its magnitude is proportional to integration time and strongly depends on temperature. Offset level and fixed pattern noise are produced by CCD electronics and therefore are independent of integration time. Dark offset can be mathematically expressed by the following equation:

$$\text{dark\_offset} = N_{DC} + N_{bias} + N_{contam}, \quad (2)$$

where N_{DC} stands for dark current. Because both offset level and fixed pattern noise are generated by CCD electronics, they are combined into a single electronic bias term, N_{bias}. The N_{contam} term accounts for possible light contamination included in dark images, such as airglow in the EV dark offset. It is produced by the CCD sensor and proportional to integration time. Because the OBCBB thermal radiation in the DNB spectral range is sufficiently weak, N_{contam} is assumed to be 0 when the BB dark offset is analyzed using Eq. (2).

As described in Section 2, the DNB EV and BB dark offset can be determined from the VROP and OBCBB data. During each monthly VROP, the DNB operates in test mode for a short time period, during which time the DNB electronics are disconnected from the DNB focal plane array. The corresponding EV and OBCBB data are then recorded under the condition of zero exposure and closed shutter, consequently measuring noise signals only due to the DNB electronics. Processing the DNB test mode data thus yields the electronic bias N_{bias} terms for both the EV and BB.

Once the dark offset and electronic bias have been determined, the relationship between the EV and BB dark offset and possible light contamination included in EV dark scenes can be analyzed via Eq. (2). Because the BB dark offset and N_{bias} are aggregation mode dependent, the EV dark offset and electronic bias are converted to the functions of aggregation mode by averaging the dark offset and electronic bias of all samples of the same aggregation mode. In this paper, the unit of dark offset, dark current, electronic bias, and the light contamination term is digital number (DN).

It is known that the DNB HGS dark offset drift is primarily due to the increase of dark current induced by radiation damage in the space environment [20]. However, as dark offset also includes electronic bias, the relationships of the EV/BB HGS dark current and the EV/BB HGS electronic bias must be analyzed separately to determine whether the BB HGS dark offset can accurately track the EV HGS dark offset drift. Direct comparison of the EV and BB HGS dark current is difficult. Because the EV HGS dark offset contains airglow whose magnitude is unknown, the corresponding EV HGS dark current

cannot be evaluated by Eq. (2). However, dark current is generated in subpixels. Only different integration times between the DNB EV and OBCBB view can lead to different dark currents. Considering that the MGS EV and BB dark offset consist of a certain amount of dark current but are free from light contamination, we used the MGS EV and BB dark current derived by Eq. (2) to investigate whether the integration time of the DNB EV and OBCBB view is the same. MGS aggregation mode 1 was selected as this aggregation mode has the most subpixels and therefore the largest dark current among all 32 aggregation modes.

The MGS EV and BB dark current of aggregation mode 1 are shown in Fig. 1. These monthly dark currents were calculated for each new moon starting on 21 February 2012 and ending on 16 January 2018. The corresponding uncertainties of the calculated dark currents are shown in the figure as well. It can be clearly seen that the time series of two dark currents are close to each other. Although their relative difference [Fig. 1(b)] is 3.67% on average, such difference is much smaller than the uncertainties shown in Fig. 1(a). Therefore, it can be assumed that there is no observable integration time difference between the DNB EV and OBCBB view. Since dark current is proportional to integration time, we can conclude that the EV and BB HGS dark current and subsequently their drift are the same. However, equal EV and BB HGS dark current drift does not guarantee equal EV and BB HGS dark offset drift. Variation of electronic bias must be considered. The EV and BB HGS electronic bias are monitored monthly through the DNB test mode during each VROP. Figure 2 shows the difference between these two electronic biases, calculated by the test mode data collected on 16 January 2018. In general, the HGS electronic bias drifts of these two views are similar for all detectors of most aggregation modes over the past six years. However, we have found a discrepancy between the EV and BB HGS electronic bias drift for a few detectors in aggregation mode 29 to 32. An example is shown in Fig. 3. From the relative change of the EV and BB HGS electronic bias of detectors 7 and 10 of aggregation mode 29 with respect to their initial values evaluated on 21 February 2012 [Fig. 3(a)], it can be seen that the electronic bias trends of the two views differ from each other from the

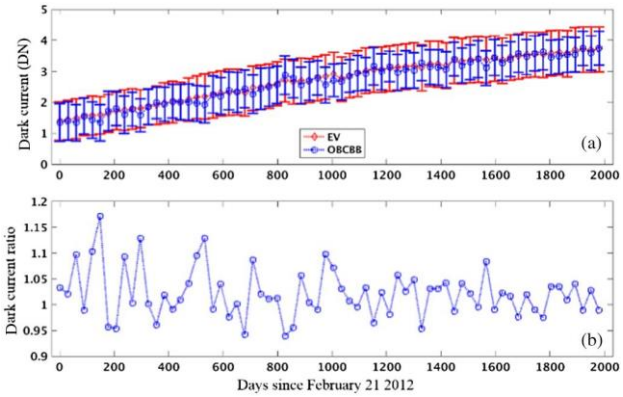

Fig. 1. (a) EV and BB MGS dark current time series. The error bars show the corresponding uncertainties of the calculated dark currents. (b) Ratios between the EV and BB MGS dark currents. Detector 1, HAM side A and aggregation mode 1.

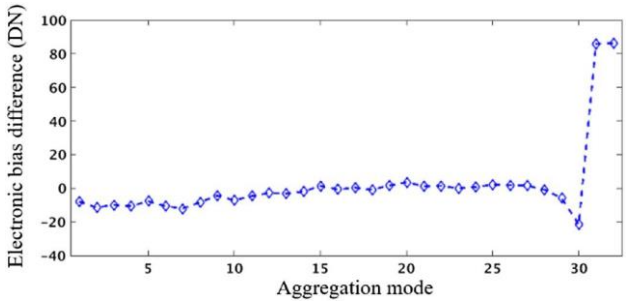

Fig. 2. Difference between the EV and BB HGS electronic bias of detector 1 on 16 January 2018 (EV—BB).

beginning of the mission; considerable discrepancy has been accumulated after years of operation. Figure 3(b) shows the change of the EV and BB HGS electronic bias between 16 January 2018 and 21 February 2012 for all 16 detectors of aggregation mode 29. The change of the EV HGS electronic bias for detectors 7 and 10 is much higher than for the rest of the detectors. In contrast, the change of the BB HGS electronic bias for detectors 7 and 10 is similar to most of the other detectors. As electronic bias is part of dark offset, such discrepancy shown in Fig. 3 eventually leads to different EV and BB HGS dark offset drift for detectors 7 and 10 of aggregation mode 29. Figure 4 shows the BB HGS dark offset drift between

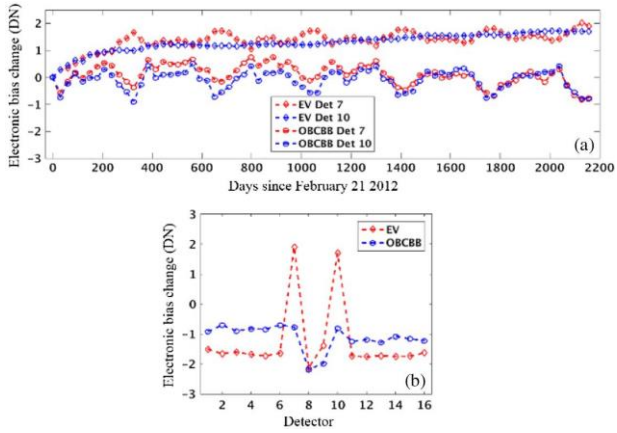

Fig. 3. (a) Relative change of the EV and BB HGS electronic bias of detectors 7 and 10 of aggregation mode 29 with respect to their initial values evaluated on 21 February 2012. (b) Change of the EV and BB HGS electronic bias between 16 January 2018 and 21 February 2012 for all detectors of aggregation mode 29.

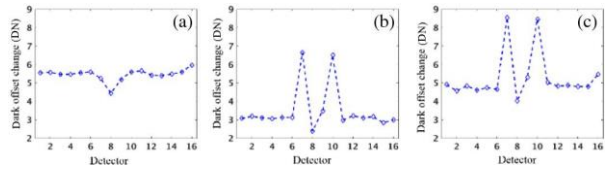

Fig. 4. (a) BB HGS dark offset drift. (b) EV HGS dark offset drift. (c) Estimated EV HGS dark offset drift. Time period is between 16 January 2018 and 21 February 2012. HAM side A, aggregation mode 29.

16 January 2018 and 21 February 2012 for all 16 detectors of aggregation mode 29 [Fig. 4(a)]. It was obtained under the linear drift model of BB HGS dark offset as assumed in the PM based algorithm [Eq. (1)]. The corresponding EV HGS dark offset drift between the same time period is shown in Fig. 4 as well [Fig. 4(b)]. Although the EV HGS dark offset drift evaluated by the VROP data is not accurate due to unknown airglow on 21 February 2012 and 16 January 2018, it can be clearly seen that the EV HGS dark offset drifts of detectors 7 and 10 are much higher than for the rest of the detectors of aggregation mode 29. However, the BB HGS dark offset drifts of detectors 7 and 10 are similar to the rest of the detectors. According to Eq. (1), the PM based algorithm uses the BB dark offset drift to estimate the EV HGS dark offset drifts. Figure 4 suggests that the EV HGS dark offset drifts of detectors 7 and 10 of aggregation mode 29 are significantly underestimated, consequently yielding striping in the calibrated DNB nighttime radiance images. In fact, the dark current parts of both EV and BB HGS dark offset are the same as they are generated in the same DNB focal plane array. The EV HGS dark offset drift can be estimated by the sum of the EV HGS electronic bias change and the BB HGS dark current change. The BB HGS dark current of a given day is evaluated by subtracting the BB HGS electronic bias from the BB HGS dark offset via Eq. (2). Figure 4(c) shows such estimated EV HGS dark offset drift between 16 January 2018 and 21 February 2012 for all detectors of aggregation mode 29. Comparison between Figs. 3(b) and 3(c) shows that combined use of the BB HGS dark current and EV HGS electronic bias can track the EV HGS dark offset drift.

The above analysis shows that the BB HGS dark offset can only track the dark current component of the DNB HGS EV dark offset, instead of the total dark offset. This relationship was revealed by subtracting the BB and EV HGS electronic bias from the corresponding dark offsets. Such subtraction makes the long-term trend of HGS dark offset appear more clearly. It is usually assumed that the BB HGS dark offsets around a new moon, which are free from the moonlight contamination, experience smooth long-term linear growth. However, in-depth examination shows that the BB HGS dark offsets do not drift linearly for mid-to-high aggregation modes. An example is shown in Fig. 5, where the aggregation mode is 28. There is almost no change in the first year and periodic drift in the following years, which may suggest spurious seasonal variations in the HGS dark offset trend. The dark currents included in the BB HGS dark offsets shown in Fig. 5 were calculated by Eq. (2). The corresponding BB HGS electronic biases of aggregation 28 used in the calculation are shown in Fig. 5 as well. It can be seen that after removing the electronic bias, the BB HGS dark current drift for this aggregation mode is linear. Our analysis of the BB HGS dark offsets of other mid-to-high aggregation modes shows similar results. Therefore, it is dark current instead of dark offset that drifts linearly.

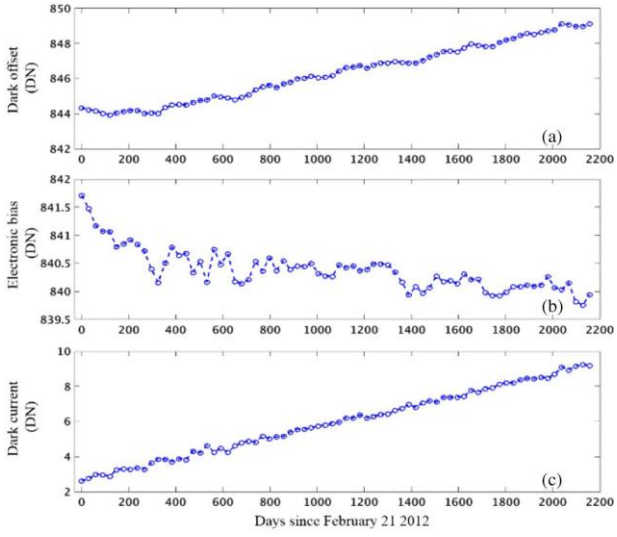

Fig. 5. (a) BB HGS dark offset time series. (b) BB HGS electronic bias time series. (c) BB HGS dark current time series. Detector 1, HAM side A and aggregation mode 28.

4. IMPROVED ALGORITHM FOR DETERMINATION OF DNB HGS DARK OFFSET

Determination of HGS dark offset that is free from light contamination is critical for the DNB low-light calibration. It relies on proper selection of a dark reference. The OBCBB is sufficiently dark when viewed by the DNB at nighttime around a new moon. In addition, it has been shown in Section 3 that the dark current component of the BB HGS dark offset can track the EV HGS dark offset change. In this section, we propose an improved algorithm to determine the EV HGS dark offset free from light contamination through combined use of the DNB OBCBB and VROP data.

The basic principle is to use the OBCBB data to estimate and then remove light contamination included in the EV HGS dark offset determined by the original algorithm that uses the VROP data. For every new moon when the DNB test mode data are available, we can calculate the BB HGS dark current by Eq. (2). Meanwhile, we can also calculate the nominal EV HGS dark current by subtracting the EV HGS electronic bias from the EV HGS dark offset determined by the original algorithm. According to Eq. (2), the nominal EV HGS dark current contains dark current and light contamination. However, the BB HGS dark current has been shown to be equal to the EV HGS dark current in Section 3. The amount of light contamination can be estimated by the difference between the nominal EV HGS dark current and the BB HGS dark current, expressed by the following equation:

$$\begin{aligned} N_{contam} = & [HGS\_dark\_offset\_EV_{orig} \\ & - HGS\_electronic\_bias\_EV] \\ & - [HGS\_dark\_offset\_BB \\ & - HGS\_electronic\_bias\_BB], \end{aligned} \quad (3)$$

where $HGS\_dark\_offset\_EV_{orig}$ is the EV HGS dark offset determined by the original algorithm. Once the estimated light contamination, N_{contam}, is known, the corrected EV HGS dark offset that is free from light contamination can be obtained by simply removing N_{contam} from the original EV HGS dark offset:

$$\text{HGS\_dark\_offset\_EV}_{\text{corr}} = \text{HGS\_dark\_offset\_EV}_{\text{orig}} - N_{\text{contam}}. \quad (4)$$

Because the BB HGS dark offset and electronic bias are defined per aggregation mode, the original EV HGS dark offset and electronic bias used in Eq. (3) are converted to functions of aggregation mode by averaging the dark offset and electronic bias of all samples of the same aggregation mode. The calculated N_{contam} is per aggregation mode. However, the EV HGS dark offset is per sample when used for calibration. N_{contam} used in Eq. (4) is converted back to functions of the sample by assigning the same value for all samples of the same aggregation mode.

Figure 6 shows the EV HGS dark offset for 20 September 2017 generated by the improved algorithm. The HGS dark offset determined by the original algorithm using the VROP data of that day and the HGS dark offset determined by the PM based algorithm [Eq. (1)] are also shown for comparison. It can be clearly seen that after removing light contamination the new dark offset is the smallest among all three versions. Our analysis shows that the bias in the EV HGS dark offset determined by the PM based algorithm comes from the baseline HGS dark offset, i.e., the first term on the right-hand side of Eq. (1). The baseline EV HGS dark offset was determined by the DNB observation of deep space collected during the spacecraft pitch maneuver on 20 February 2012, one day before the first VROP. Upon rotation of the spacecraft around its pitch axis, the DNB can view deep space through the EV [21]. Although deep space is free from airglow, it contains electromagnetic radiation emitted by stars, referred to as starlights. In fact, several bright pixels that are images of stars are observed in the collected DNB deep space scene.

The amount of starlight contamination can be estimated by the basic principle of our proposed new algorithm [Eq. (3)]. We first calculated the BB HGS dark current on 21 February 2012 through Eq. (2). By assumption of the negligible dark current change over one day, it is also approximately the BB HGS dark current for 20 February 2012, the day on which the spacecraft pitch maneuver was performed. Meanwhile, we also calculated the nominal EV HGS dark current on 20 February 2012 by subtracting the EV HGS electronic bias on 21 February 2012 from the baseline EV HGS dark offset. Here we also assume negligible change of the EV

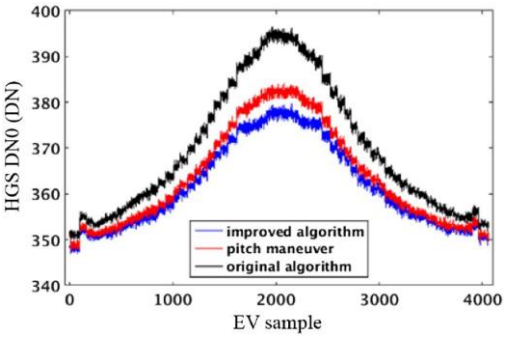

Fig. 6. EV HGS dark offset (DN0) for 20 September 2017. Detector 1, HAM side A.

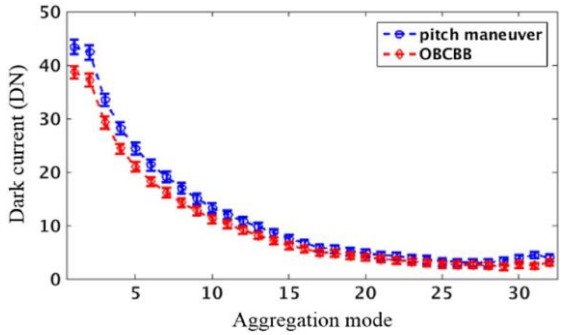

Fig. 7. BB HGS dark current included in the BB HGS dark offset for 21 February 2012 and the nominal EV HGS dark current included in the baseline EV HGS dark offset determined by the DNB pitch maneuver data collected on 20 February 2012. Detector 1 and HAM side A.

HGS electronic bias over one day. Both HGS dark currents are shown in Fig. 7. Error bars indicate the corresponding uncertainties of the calculated dark currents. It can be clearly seen that the nominal EV HGS dark current is higher than the BB HGS dark current for all aggregation modes. Since we have shown the same EV and BB HGS dark current, the difference exhibited in Fig. 7 suggests nonzero starlight contamination included in the baseline EV HGS dark offset determined by the DNB deep space scenes collected during the spacecraft pitch maneuver. It is worth mentioning that we adopted a proper filtering scheme to remove bright star pixels when processing the DNB pitch maneuver data to compute the baseline EV HGS dark offset. However, space is an environment full of electromagnetic fields radiated by various sources such as stars. Due to the extreme sensitivity of the DNB HGS, these weak electromagnetic fields become detectable, resulting in the elevated baseline EV HGS dark offset.

It has been shown that the DNB is able to image cloud and surface features by airglow, starlight, and zodiacal light illumination in the range from 10^{-11} to 10^{-9} W · cm^{-2} · sr^{-1} · μm^{-1} [3]. Under such low-light conditions, the internal light scattering inside the VIIRS optical system is negligible according to the prelaunch testing [22]. The different dark currents shown in Fig. 7 indicate that the starlight contamination included in the EV HGS dark offset is on the order of 10^{-11} W · cm^{-2} · sr^{-1}. Therefore removal of this bias by our improved algorithm is beneficial for the DNB's environmental sensing capabilities at nighttime.

A DNB nighttime image of the Western United States calibrated by the new EV HGS dark offset is shown in Fig. 8. Although there is no qualitative difference compared to the DNB image of the same area calibrated by the EV HGS dark offset that was generated by the PM based algorithm, histograms of the two radiance images reveal the difference. As shown in Fig. 8(b), radiances at the level below 10^{-9} W · cm^{-2} · sr^{-1} are lifted in the image using the new dark offset. The average radiance over the San Mateo Bridge that crosses San Francisco Bay [Fig. 8(c), blue dots] is 4.36×10^{-9} W · cm^{-2} · sr^{-1}, increased by 1.51% compared to the one calibrated by the EV HGS dark offset determined by the PM based algorithm [Eq. (1)].

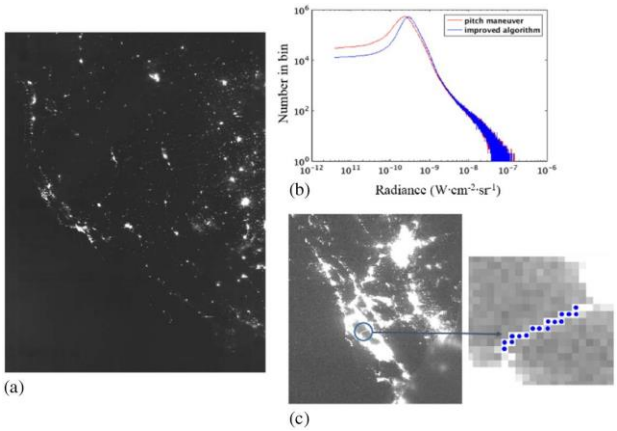

Fig. 8. (a) DNB nighttime image of the Western United States on 21 September 2017. (b) Histograms of the DNB nighttime radiance images shown in (a) calibrated by the EV HGS dark offsets determined by the PM based algorithm (red) and the improved algorithm (blue). (c) DNB nighttime image of the San Mateo Bridge that crosses San Francisco Bay on 21 September 2017.

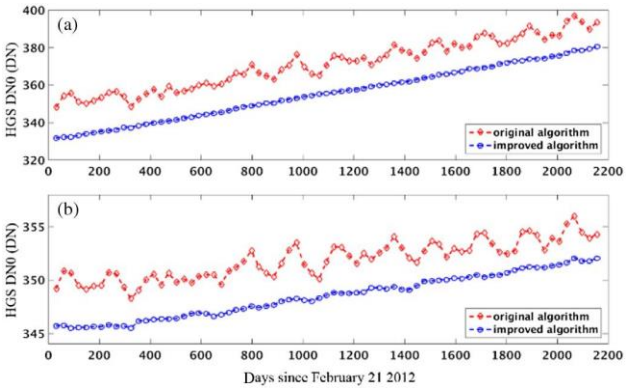

Fig. 9. (a) EV HGS dark offset (DN0) time series determined by the original and improved algorithm. Detector 1, HAM side A, and aggregation mode 1. (b) EV HGS dark offset (DN0) time series determined by the original and improved algorithm. Detector 1, HAM side A, and aggregation mode 25.

We have reprocessed the historical VROP data to generate the EV HGS dark offsets free from light contamination by our improved algorithm. The results are shown in Fig. 9, where the time series of the EV HGS dark offset determined by the original algorithm using the VROP data is also shown. Short-term fluctuations, exhibited in the original one, have been significantly reduced in the new one. This is attributed to the OBCBB's high stability. Smooth long-term drift of the EV HGS dark offset determined by the improved algorithm could potentially improve the DNB radiometric performance at low radiance level.

5. CONCLUSIONS

In this paper, we have comprehensively analyzed the relationship between the DNB EV and BB HGS dark offset. Our analysis shows that the BB HGS dark current, which is part of the BB HGS dark offset, must be used with the EV electronic bias to track the on-orbit change of the EV HGS dark offset. We have also shown that the OBCBB at nighttime around a new moon is the darkest target available for the DNB EV HGS dark offset determination, better than either deep space or the Pacific Ocean during nighttime of the new moon.

With this acquired knowledge, an improved algorithm was proposed to determine the DNB HGS dark offset. The improved algorithm does not require the DNB data collected during the spacecraft pitch maneuver. By combined use of the DNB OBCBB data and the DNB VROP data, the generated EV HGS dark offset is free from light contamination and consequently increases smoothly over the whole mission. The improved algorithm could potentially improve the DNB radiometric performance at low radiance level and benefit its environmental sensing capabilities at nighttime.

Although the work presented in this paper is focused on the DNB HGS dark offset calibration, it is also applicable for the DNB MGS and LGS dark offset calibration. The difference between the BB and EV electronic bias of the MGS and LGS must be considered if the BB MGS and LGS dark offset are used to track the EV MGS and LGS dark offset change. In general, our results provide a solid theoretical basis for dark offset calibration of the VIIRS DNB onboard the S-NPP satellite and the following Joint Polar Satellite System (JPSS) satellites.

The DNB EV and BB electronic bias are critical for the improved algorithm. They are generated by the DNB electronics, depending on the electronic timing mode. The relationship between the DNB EV and BB dark offset, originally concealed by the different electronic timing, was revealed after the removal of the EV and BB electronic bias from them. The dark current components of the two dark offsets are the same. Since the BB HGS dark offset is not contaminated, any detected weak light hidden in the EV HGS dark offset determined by the DNB scenes of either deep space or the Pacific Ocean during nighttime of a new moon can be identified and eliminated by using the BB HGS dark current.

However, determination of the DNB EV and BB electronic bias relies on the data collected when the DNB operates in the test mode. This is a nonoperational mode, currently enabled for a short time period during monthly VROP. An offline data process is required to determine the EV and BB electronic bias. As shown in Section 3, the HGS EV and BB electronic bias vary differently for certain detectors of several aggregation modes for the S-NPP VIIRS DNB. In addition, their variation over time cannot be simply modeled by linear or nonlinear fitting. A periodic check of the EV and BB electronic bias through the test mode is necessary for accurate HGS EV dark offset calibration. Such experience suggests that the EV and BB electronic bias must be well characterized before considering automatic dark offset calibration for all gain stages of the VIIRS DNB onboard the following JPSS satellite.

Funding. National Oceanic and Atmospheric Administration (NOAA); Joint Polar Satellite System program office.

Acknowledgment. This paper's contents are solely the opinions of the authors and do not constitute a statement of policy, decision, or position on behalf of NOAA or the U.S. government.

REFERENCES

1. C. Cao, J. Xiong, S. Blonski, Q. Liu, S. Uprety, X. Shao, Y. Bai, and F. Weng, "Suomi NPP VIIRS sensor data record verification, validation, and long-term performance monitoring," J. Geophys. Res. 118, 11644–11678 (2013).
2. L. B. Liao, S. Weiss, S. Mills, and B. Hauss, "Suomi NPP VIIRS day-night band on-orbit performance," J. Geophys. Res. 118, 12705–12718 (2013).
3. S. D. Miller, S. P. Mills, C. D. Elvidge, D. T. Lindsey, T. F. Lee, and J. D. Hawkins, "Suomi satellite brings to light a unique frontier of night-time environmental sensing capabilities," Proc. Natl. Acad. Sci. USA 109, 15706–15711 (2012).
4. S. D. Miller, W. Straka III, S. P. Mills, C. D. Elvidge, T. F. Lee, J. Solbrig, A. Walther, A. K. Heidinger, and S. C. Weiss, "Illuminating the capabilities of the Suomi National Polar-Orbiting Partnership (NPP) visible infrared imaging radiometer suite (VIIRS) day/night band," Remote Sens. 5, 6717–6766 (2013).
5. C. D. Elvidge, K. Baugh, M. Zhizhin, F. C. Hsu, and T. Ghosh, "VIIRS night-time lights," Int. J. Remote Sens. 38, 5860–5879 (2017).
6. M. O. Román, Z. Wang, Q. Sun, V. Kalb, S. D. Miller, A. Molthan, L. Schultz, J. Bell, E. C. Stokes, B. Pandey, K. C. Seto, D. Hall, T. Oda, R. E. Wolfe, G. Lin, N. Golpayegani, S. Devadiga, C. Davidson, S. Sarkar, C. Praderas, J. Schmaltz, R. Boller, J. Stevens, O. M. R. González, E. Padilla, J. Alonso, Y. Detrés, R. Armstrong, I. Miranda, Y. Conte, N. Marrero, K. MacManus, T. Esch, and E. J. Masuoka, "NASA's Black Marble nighttime lights product suite," Remote Sens. Environ. 210, 113–143 (2018).
7. C. Cao, X. Shao, and S. Uprety, "Detecting light outages after severe storms using the S-NPP/VIIRS Day/Night Band radiances," IEEE Geosci. Remote Sens. Lett. 10, 1582–1586 (2013).
8. C. D. Elvidge, M. Zhizhin, K. Baugh, and F. C. Hsu, "Automatic boat identification system for VIIRS low light imaging data," Remote Sens. 7, 3020–3036 (2015).
9. J. Geis, C. Florio, D. Moyer, K. Rausch, and F. de Luccia, "VIIRS day-night band gain and offset determination and performance," Proc. SPIE 8510, 851012 (2012).
10. S. Uprety, C. Cao, Y. Gu, and X. Shao, "Improving the low light radiance calibration of S-NPP VIIRS Day/Night Band in the NOAA operations," in *IEEE International Geoscience and Remote Sensing Symposium (IGARSS)*, July 2017, pp. 4726–4729.
11. S. Lee, K. Chiang, X. Xiong, C. Sun, and S. Anderson, "The S-NPP VIIRS day-night band on-orbit calibration/characterization and current state of SDR products," Remote Sens. 6, 12427–12446 (2014).
12. S. Lee, J. McIntire, H. Oudrari, T. Schwarting, and X. Xiong, "A new method for Suomi-NPP VIIRS day-night band on-orbit radiometric calibration," IEEE Trans. Geosci. Remote Sens. 53, 324–334 (2015).
13. X. Xiong, J. Butler, K. Chiang, B. Efremova, J. Fulbright, N. Lei, J. McIntire, H. Oudrari, Z. Wang, and A. Wu, "Assessment of S-NPP VIIRS on-orbit radiometric calibration and performance," Remote Sens. 8, 84 (2016).
14. H. Chen, X. Xiong, C. Sun, X. Chen, and K. Chiang, "Suomi-NPP VIIRS day-night band on-orbit calibration and performance," J. Appl. Remote Sens. 11, 036019 (2017).
15. "Joint Polar Satellite Systems VIIRS Radiometric Calibration Algorithm Theoretical Basis Document," Revision D, 2017, https://www.star.nesdis.noaa.gov/jpss/documents/ATBD/D0001-M01-S01-003_JPSS_ATBD_VIIRS-SDR_D.pdf.
16. X. Xiong, J. Butler, K. Chiang, B. Efremove, J. Fulbright, N. Lei, J. McIntire, H. Oudrari, J. Sun, Z. Wang, and A. Wu, "VIIRS on-orbit calibration methodology and performance," J. Geophys. Res. 119, 5065–5078 (2014).
17. "Joint Polar Satellite System VIIRS Geolocation Algorithm Theoretical Basis Document," Revision A, 2017, https://www.star.nesdis.noaa.gov/jpss/documents/ATBD/D0001-M01-S01-004_JPSS_ATBD_VIIRS-Geolocation.pdf.
18. C. Sun, T. Schwarting, H. Chen, K. Chiang, and X. Xiong, "Prediction of S-NPP VIIRS DNB gains and dark offsets," Proc. SPIE 10402, 104021U (2017).
19. G. R. Hopkinson, T. M. Goodman, and S. R. Prince, *A Guide to the Use and Calibration of Detector Array Equipment* (SPIE, 2004).
20. A. Yamashita, T. Dotani, M. Bautz, G. Crew, H. Ezuka, K. Gendreau, T. Kotani, K. Mitsuda, C. Otani, A. Rasmussen, G. Ricker, and H. Tsunemi, "Radiation damage to charge coupled devices in the space environment," IEEE Trans. Nucl. Sci. 44, 847–853 (1997).
21. J. J. Butler, X. Xiong, R. A. Barnes, F. S. Patt, J. Sun, and K. Chiang, "An overview of Suomi NPP VIIRS calibration maneuvers," Proc. SPIE 8510, 85101J (2012).
22. H. Oudrari, J. McIntire, X. Xiong, J. Bulter, Q. Ji, T. Schwarting, S. Lee, and B. Efremova, "JPSS-1 VIIRS radiometric characterization and calibration based on pre-launch testing," Remote Sens. 8, 41 (2016).